Check for updates

Superparamagnetic nanoparticles as potential *drug delivery* systems for the treatment of Duchenne muscular dystrophy†

Maria L. Schumacher,[a] Tatiane N. Britos,[a] Fernando L. A. Fonseca,[b]
Fabio F. Ferreira, [ID] [c,d] David Feder,[b] Paula Fratini,[b] Giuliana Petri[b] and
Paula S. Haddad [ID] *[a]

This study aims to use superparamagnetic iron oxide nanoparticles (SPIONs), specifically magnetite (Fe_3O_4), to deliver deflazacort (DFZ) and ibuprofen (IBU) to Duchenne muscular dystrophy-affected (DMD) mouse muscles using an external magnetic field. The SPIONs are synthesized by the co-precipitation method, and their surfaces are functionalized with L-cysteine to anchor the drugs, considering that the cysteine on the surface of the SPIONs in the solid state dimerizes to form the cystine molecule, creating the Fe_3O_4-$(Cys)_2$-DFZ and Fe_3O_4-$(Cys)_2$-IBU systems for *in vivo* tests. The Fe_3O_4 nanoparticles (NPs) were characterized by Fourier transform infrared spectroscopy (FTIR), Raman spectroscopy, powder X-ray diffraction (PXRD), transmission electron microscopy (TEM), dynamic light scattering (DLS), and magnetic measurements. The results show that the SPIONs have an average crystallite size of about 8 nm in the solid state and a hydrodynamic size of about 120 nm, which is suitable for biological applications in aqueous dispersion. The nanoparticles exhibit superparamagnetic behavior at room temperature and spherical-close morphology. In addition, vibrational modes characteristic of the functional groups of the molecules anchored to the surface of the SPIONs are identified. Data from blood tests of *mdx* mice after seven consecutive days of treatment with nanoparticles confirm the non-toxic nature of the system and show an improvement in DMD, with normal levels of liver and kidney enzymes and a decrease in creatine kinase protein.

1. Introduction

Duchenne muscular dystrophy (DMD) is an X-linked genetic disease caused by a mutation in the dystrophin gene, primarily affecting male children at a rate of 1 in 3500 to 5000 newborns worldwide.[1] Although there is phenotypic variability, the clinical signs of the disease begin to be noticeable between the ages of 2 and 5, with delays in motor milestones, falls, walking on toes, calf hypertrophy, very high creatine kinase (CK) levels, and typically, mild cognitive impairment, making a diagnosis possible in conjunction with a genetic test.[1] The disease rapidly progresses, leading to complete loss of motor functions by age 10, followed by cardiac and respiratory complications by age 20, which are the main cause of death.[2,3]

Currently, there is no cure for DMD. Standard treatment typically involves immunosuppressant medications such as corticosteroids (deflazacort and prednisone) and anti-inflammatory drugs (ibuprofen) to alleviate symptoms. Corticosteroids are commonly prescribed to help maintain muscle strength in patients. However, long-term use of these medications can result in serious side effects, including leg swelling, glaucoma, depression, high blood pressure, high blood sugar, osteoporosis, osteonecrosis, and fractures.[4–6] New therapeutic proposals based on the replacement or modification of genetic material and the repurposing of drugs have been developed in medicine to replace the use of immunosuppressants.[4–9] Therapy based on restoring dystrophin function by adding genes through exon skipping is an innovative alternative. In this case, an antisense oligonucleotide is used to prevent the production of the dystrophin protein from being interrupted when it encounters a mutation, causing mutant exons to be skipped.[10]

Nonetheless, due to the complexity associated with these types of treatment, several pre-clinical studies are needed

[a]Department of Chemistry, Federal University of São Paulo (UNIFESP), Diadema, SP, Brazil. E-mail: haddad.paula@unifesp.br
[b]Faculty of Medicine of ABC (FMABC), Santo André, SP, Brazil
[c]Center for Natural and Human Science (CCNH), Federal University of ABC (UFABC), Santo André, SP, Brazil
[d]Nanomedicine Research Unit (NANOMED), Federal University of ABC (UFABC), Santo André, SP, Brazil
†Electronic supplementary information (ESI) available. See DOI: https://doi.org/10.1039/d4nr03407d

before they can be released, making it difficult for patients to access them. In this context, nanoparticulate materials are of great interest in the medical field due to their specific properties on the nanoscale that allow for the treatment, diagnosis, and transportation of drugs in the living organism.[11–14] Among nanomaterials, superparamagnetic iron oxide nanoparticles (SPIONs) are widely used in a variety of biomedical applications due to the proven biocompatibility of iron in a specific concentration range and their magnetic characteristics, which differ from other materials due to the so-called superparamagnetism effect.[15]

Manufacturing superparamagnetic magnetite nanoparticles (SPIONs) in compliance with Good Manufacturing Practices (GMP) requires advanced infrastructure and high operational costs. To meet regulatory requirements, specialized facilities with classified cleanrooms must be implemented to minimize contamination and ensure product quality. Specific equipment, such as closed reactors, high-precision purification systems, and advanced characterization instruments (e.g., DLS, spectroscopy, and trace metal analysis), is essential. Moreover, each step of the synthesis and functionalization process must be validated to ensure the produced nanoparticles' consistency, reproducibility, and safety.

The costs associated with GMP compliance include not only the initial investment in infrastructure and equipment but also ongoing expenses for staff training, regular audits, and maintenance. It is crucial to train operators and scientists to work in controlled environments and perform rigorous quality testing, including sterility, toxicity, and stability assays. Additionally, the process must be meticulously documented, as regulatory agencies like ANVISA, EMA, and FDA require full traceability.

Another key aspect is post-production quality control, which involves frequent and thorough analyses to ensure batches meet established standards. While initial costs are high, investing in GMP compliance is essential to ensure SPIONs are safe and effective for medical applications, such as clinical trials. This investment enhances the product's credibility and acceptance by the scientific and medical communities, while also opening doors to commercialization in regulated markets.

In this context, the co-precipitation method in laboratory settings offers a cost-effective alternative for the initial synthesis of SPIONs. Due to its simplicity, low cost, and high adaptability, it allows for the development and optimization of nanoparticles on a small scale before committing to GMP-compliant production infrastructure. Furthermore, the co-precipitation method is well-suited for exploring synthesis and functionalization parameters, ensuring reproducible results that can later be scaled to meet regulatory requirements. Thus, it serves as a crucial and economical step in advancing SPION research and development toward clinical applications.

Some examples of applications are in the field of imaging, such as magnetic resonance imaging (MRI),[16] X-ray imaging[17] and, more recently, magnetic particle imaging (MPI);[18] in magnetic hyperthermia treatments (MHT);[19] in controlled drug release, where they act as "drug delivery",[20] in cancer treatment and human tissue repair,[21] where they are used to track, direct and locate stem cells to the site of tissue damage.

Most of these applications require functionalizing the SPIONs' surface with suitable biomolecules to enable the chemical conjugation of ligands and drugs. Coating and functionalizing the surface of SPIONs can help address issues related to their stability in colloidal solutions and biological fluids.[22–25] Biomolecules on the surface of SPIONs allow them to remain in the bloodstream for longer periods, reducing the formation of magnetic aggregates that can cause thrombosis and blood clots.[23] In addition, functionalization makes it possible to target specific treatment sites and prevents healthy cells from interacting with tissues and drug transporters. Different materials, such as biocompatible polymers, amino acids, surfactants, liposomes, and homing cells, can coat superparamagnetic nanoparticles.[22]

L-Cysteine (Cys) is one of the most important antioxidants in vivo, protecting cells against reactive oxygen species generated during oxidative stress.[24] Its chemical structure (Fig. 1a) includes carboxylic acid (–COOH), thiol (–SH), and amine organic groups (–NH$_2$) that can interact strongly with metals and metal complexes, facilitating the production and functionalization of new nanoparticles.[25] Studies have shown that the carboxylate group of cysteine can form either monodentate or bidentate complexes with metal ions, including iron. In the case of magnetite, cysteine can also interact through its thiol group (–SH), but the carboxylate group is particularly significant, especially in conditions where the thiol
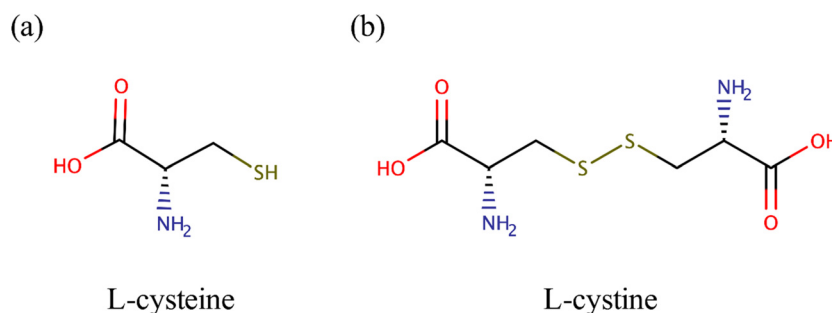

Fig. 1 Chemical structure of (a) L-cysteine and (b) L-cystine.

group is less reactive.[26,27] Furthermore, in the biomedical field, these groups enable drug administration, detoxification, modification, and protein synthesis.[28]

Previous studies by the group have confirmed the adsorption of the cysteine molecule onto the metal surface through the carboxylate group ($-COO^-$), resulting in magnetite nanoparticles with free thiol groups, which hold potential for use in drug delivery systems.[29,30] However, when these nanoparticles (NPs) are in a solid state, it was observed that L-cysteine undergoes dimerization to form an L-cystine crystal structure ($(Cys)_2$), as illustrated in Fig. 1b. This occurs due to the redox environment created by the Fe^{3+} and Fe^{2+} ions in the magnetite.[27]

The ability of SPIONs to respond to external magnetic fields allows for their controlled targeting of specific areas of the body, enhancing the precision and effectiveness of drug delivery while reducing side effects.[30] Thus, by conjugating drugs to the functionalized surface of SPIONs, treating diseases that do not yet have a 100% effective therapy, as with Duchenne muscular dystrophy, is possible.

There is research in the literature on the use of SPIONs in treating Duchenne muscular dystrophy, including stem cell therapy;[31–33] however, few studies address the *in vivo* application of these systems as drug transporters. Stem cell therapy involves introducing healthy stem cells into the affected tissue to replace or repair damaged muscle cells. SPIONs play a crucial role in enabling the visualization and tracking of these stem cells during treatment. Due to their iron composition, SPIONs can be detected using magnetic resonance imaging (MRI). This allows for the non-invasive monitoring of the injected stem cells in the muscle tissue affected by DMD.

Therapies utilizing genetic modifications and tissue engineering, such as the insertion of stem cells, are complex and expensive to develop. They also require extensive pre-clinical studies before being approved for human use. To propose a more effective and accessible treatment, this study focused on integrating SPIONs into the conventional treatment of DMD, which involves continuous administration of corticosteroids. In this approach, SPIONs act as drug transport vehicles, allowing direct delivery of the drug to the site affected by DMD. This process enhances the effectiveness of the active ingredient at the specific site while minimizing side effects in the body. Therefore, in this work, we investigated the preparation, characterization, and application of L-cysteine-functionalized magnetite nanoparticles for drug delivery in the treatment of DMD. The main goal was to target deflazacort and ibuprofen in the muscles of mice containing Duchenne muscular dystrophy.

2. Materials and methods

2.1. Materials

Deflazacort ($C_{25}H_{31}NO_6$), ibuprofen ($C_{13}H_{18}O_2$), L-cysteine ($C_3H_7NO_2S$), iron(III) chloride hexahydrate, ($FeCl_3\cdot6H_2O$), iron

(II) chloride tetrahydrate ($FeCl_2\cdot4H_2O$), ammonium hydroxide (NH_4OH), 5,5′-dithiobis 2-nitrobenzoic acid (DTNB), TRIS borate – EDTA buffer solution pH 8.3, ethylenediaminetetraacetic acid ($C_{10}H_{16}N_2O_8$ – EDTA), were acquired from Sigma-Aldrich, Inc., USA and used as received. Manipulated deflazacort (25 mg, 12 wt%) was obtained from Essencial Pharmacy (Santo André, São Paulo, Brazil). Manipulated ibuprofen (500 mg, 100 wt%) was obtained from Formulas Pharmacy (Santo André, São Paulo, Brazil). Aqueous solutions were prepared using analytical-grade water from a Millipore Milli-Q Gradient filtration system.

Healthy and dystrophic (*mdx*) C57BL/10 mice were obtained from the Animal Vivarium of the Faculty of Medicine of ABC (FMABC). Neodymium magnetic pads (diameter 4 × 2 mm) were obtained from Oximag. Isoflurane 0.2% was used to anesthetize the animals, while pentobarbital sodium was used to euthanize them.

2.2. Methods

2.2.1. Synthesis of SPIONs.[34] Fe_3O_4 nanoparticles were synthesized in an aqueous medium using the co-precipitation method.[34] A solution containing 4.0 mL of $FeCl_3\cdot6H_2O$ (1 mol L^{-1}) and 1.0 mL of $FeCl_2\cdot4H_2O$ (0.5 mol L^{-1}) was prepared in HCl (1 mol L^{-1}). This mixture was continuously stirred magnetically while 50 mL of NH_4OH (0.7 mol L^{-1}) was gradually added. The black precipitate formed was magnetically decanted and washed ten times with ethanol, resulting in Fe_3O_4 nanoparticles. The ethanol used in washing the precipitate is allowed to evaporate completely in a desiccator, a process that is widely adopted in scientific literature due to the high volatility of ethanol. Based on the storage time and controlled conditions in the desiccator, we estimate that evaporation is effective in removing most of the residual ethanol. This practice is well-established, and although evaporation does not automatically eliminate other residual solvents, the use of ethanol alone, which has a low boiling point and high volatility, makes it unlikely that significant amounts of other solvents remain.

2.2.2. SPIONs functionalization with L-cysteine. Fe_3O_4 nanoparticles (100 mg) were dispersed in 5 mL of water, and 500 mg of L-cysteine were dissolved in 5 mL of water. The dispersion (Fe_3O_4 nanoparticles) and the solution (L-cysteine) were stirred continuously for 14 hours, producing a brown precipitate that was magnetically decanted and washed ten times with ethanol. This procedure resulted in the obtention of $Fe_3O_4\text{-}(Cys)_2$ nanoparticles.

2.2.3. Anchoring of drugs on the surface of $Fe_3O_4\text{-}(Cys)_2$. A mass of 200 mg of $Fe_3O_4\text{-}(Cys)_2$ nanoparticles was dispersed in 10 mL of water, and 1 g of the deflazacort was dispersed in 10 mL of water to achieve the mass ratio SPIONs : drug = 1 : 5. The two dispersions were mixed and stirred for 24 hours at room temperature, resulting in a brown precipitate. This precipitate was magnetically decanted and washed 10 times with ethanol, resulting in the $Fe_3O_4\text{-}(Cys)_2\text{-}DFZ$ system. The same procedure was carried out to anchor ibuprofen to the SPIONs, forming $Fe_3O_4\text{-}(Cys)_2\text{-}IBU$.

It is worth emphasizing that the samples were stored in a desiccator for several days during the synthesis and storage of the described compounds to ensure complete ethanol removal and allow for the complete evaporation of any residual solvent.

2.2.4. Fourier transform infrared spectroscopy (FTIR) and Raman spectroscopy. FTIR spectra were obtained using the Agilent Cary 630 spectrometer with an ATR accessory made of diamond crystal. The measurements were carried out from 400 to 4000 cm^{-1}, with a resolution of 4 cm^{-1} and 512 scans.

Raman spectroscopy measurements were carried out on a Renishaw InVia microscope, using radiation at 632.8 nm (He–Ne laser), with an exposure time of 30 s, 3 acquisition accumulations, and a laser power of 1% with 15 mW incident on the sample. Before analysis, the fine, homogeneous powder obtained from macerating the sample was dried under the illumination of a UV lamp for 15 minutes.

2.2.5. Powder X-ray diffraction (PXRD). Powder X-ray diffraction analyses (Fe$_3$O$_4$-(Cys)$_2$, Fe$_3$O$_4$-(Cys)$_2$-DFZ, and Fe$_3$O$_4$-(Cys)$_2$-IBU) were performed using a STADI-P diffractometer (Stoe® Darmstadt, Germany) in transmission geometry (the samples were deposited between two cellulose acetate foils), with the diffractometer operating at 40 kV and 40 mA and equipped with a Ge (111) primary beam monochromator, providing AgKα1 radiation (λ = 0.55941 Å). The X-ray photons were detected by a Mythen2 1K detector (Dectris®, Baden, Switzerland) in the range from 4° to 50° (2θ) with a step size of 0.015° (2θ) and integration time of 120 s per 3.15°. L-Cysteine, deflazacort, and ibuprofen were analyzed using an STADI-P X-ray diffractometer (Stoe®, Darmstadt, Germany) with transmission geometry. The diffractometer utilized CuKα1 radiation (λ = 1.54056 Å) at 40 kV and 40 mA and was equipped with a Ge (111) primary beam monochromator. X-ray photons were detected by a Mythen 1K detector (Dectris®, Baden, Switzerland) in the range from 2° to 90° (2θ), with a step size of 0.015° (2θ) and an integration time of 120 seconds per 3.15°. The resulting data were analyzed using TOPAS-Academic V7 software to quantify the phases through Rietveld refinements. The crystal structures were referenced from the Inorganic Crystal Structure Database (ICSD) and QualX2 software, which utilizes an internal Crystallography Open Database (COD) version.

2.2.6. Transmission electron microscopy (TEM). The morphology and size distribution of the superparamagnetic NPs were identified using a Talos F200X G2 Transmission Electron Microscope with cold gun field-effect emission (FEG-X), scanning module (STEM), and atomic resolution capability (HRTEM). The samples were suspended in ethanol, and then a drop of the supernatant dispersion was deposited on an amorphous carbon film supported by a copper grid. The size distribution and average diameter were calculated from 250 nanoparticles.

2.2.7. Magnetization measurements. The magnetic characterizations were performed at 300 K using a Quantum Design EverCool II PPMS device with a VSM (Vibrating-Sample Magnetometer). The measurements obtained were magnetization *versus* the applied magnetic field, ranging from −0.3 to 0.3 Tesla for the Fe$_3$O$_4$-(Cys)$_2$-IBU sample and from −1.0 to 1.0 Tesla for the other samples, allowing for the construction of the hysteresis loop of the synthesized materials. The measurements were carried out on dried powders, lightly pressed, and conditioned in lucite cylindrical holders.

2.2.8. Dynamic light scattering and zeta potential. Dynamic light scattering measurements were performed using a compact ALV/CGS-3 goniometer system consisting of a 22 mW linearly polarized He–Ne laser operating at a wavelength of λ = 633 nm, an ALV 7004 digital correlator and a pair of avalanche photodiodes operating in the pseudocross correlation mode. Autocorrelation functions were obtained in the 90° angle region and adjusted using the cumulative method. The Zeta Potential of the synthesized samples was measured on the Zetasizer Nano ZS, Malvern Instruments, using the electrophoretic light scattering (ELS) technique. The suspensions were prepared for both analyses by dispersing approximately 10 mg of the sample in 20 mL of water using ultrasound at a consistent temperature of 25 ± 1 °C.

2.2.9. Quantification of free thiol groups on the surface of SPIONs. The thiol groups (–SH) on the surface of the nanoparticles were quantified by titration with 5′,5′-ditiobis-(2-nitrobenzoic acid) (DTNB) using the ultraviolet-visible spectrophotometry technique. The free –SH reacts with DTNB to form 5-mercapto-2-nitrobenzoic acid (TNB^{2-}) with a characteristic absorption band at 412 nm (ε = 11 400 M^{-1} cm^{-1}). Briefly, 10 mg of NPs was dispersed in 1.5 mL of TBE buffer (TRIS-borate EDTA) and added to 200 μL of DTNB (5.07 mmol L^{-1}) in TBE buffer (pH 8.3) with 1 mmol L^{-1} of ethylenediaminetetraacetic acid (EDTA). After 5 minutes of incubation, the suspensions were centrifuged. The supernatant was placed in a quartz cuvette, and the absorption band at 412 nm was measured using a UV-Vis spectrophotometer (Agilent, model 8553). The experiments were carried out in triplicate, and the standard deviation was estimated.

2.2.10. Quantification of deflazacort and ibuprofen adsorbed on Fe$_3$O$_4$-(Cys)$_2$. The quantification of the drugs deflazacort and ibuprofen was carried out at the Laboratory of Crystallography and Structural Characterization of Materials (LCCEM) at UFABC using a quantitative phase analysis (QPA) procedure [**https://doi.org/10.1107/S0021889887086199** e **https://doi.org/10.1107/S0021889887009415**] using the Rietveld method [**https://doi.org/10.1107/S0021889869006558**] implemented in the TOPAS-Academic V7 [**https://doi.org/10.1107/S1600576718000183**] software. Qualitative phase analysis was carried out using the QualX2 software [**https://doi.org/10.1107/S1600576715002319**], which uses a compiled version of the Crystallography Open Database (COD) [**https://doi.org/10.1093/nar/gkr900**].

2.3. *In vivo* assays

To conduct the *in vivo* assays, we submitted a project to the FMABC Animal Ethics Committee, approved under number 16/2022. The project complies with the provisions of Law 11 794 of October 8, 2008, and Decree 6899 of July 15, 2009, and the regulations issued by the National Council for the

Control of Animal Experimentation (CONCEA). Approval was granted on November 17, 2022, by the Ethics Committee on Animal Use (CEUA) of the FMABC University Center.

2.3.1. Animals. In the *in vivo* studies, 60-day-old male isogenic C57BL/10 mice (healthy control animals, designated as black) and isogenic *mdx* mice (mutant strain used to study muscular dystrophy) were used. The animals were maintained in the Animal Vivarium of FMABC under a 12 h light cycle, with controlled temperature and humidity, and received filtered water and Nuvital CR-1 food *ad libitum*.

The animals were divided into 8 different groups (*n* = 6), using various types of treatment, as described in Table 1. The Sham groups consisted of black and *mdx* animals treated only with sterile saline NaCl 0.9% (9 mg mL^{-1}).

2.3.2. Magnet implantation. The animals underwent inhalation anesthesia to implant the subcutaneous magnet with 2% isoflurane. A trichotomy was performed, and a small cut was made in the skin above the quadriceps muscle, where the magnet was implanted, and the skin closed with tissue glue. Since the procedure is minimally invasive, no analgesic was administered. The treatments were performed after the magnet implantation.

2.3.3. Assessing methodology. Initially, tests were carried out to assess the nanoparticle's toxicity and evaluate the effects of magnet implantation without the drugs deflazacort and ibuprofen. To this end, tests were carried out using groups 1, 2, 3, and 4 in Table 1.

The groups were kept for 7 days under the conditions, with free access to water and food. Groups 3 and 4 received a daily intraperitoneal injection (7 days) of the nanoparticle (1000 µg mL^{-1}, 0.5 mL per injection) dispersed in saline solution (0.9% NaCl). The animals in group 5 received deflazacort at a concentration (660 µg mL^{-1}), group 6 received ibuprofen at a concentration (896 µg mL^{-1}), group 7 received nanoparticles with deflazacort at a concentration (1000 µg mL^{-1}) and group 8 received nanoparticles with ibuprofen at a concentration (1000 µg mL^{-1}).

2.3.4. Blood and muscle collection. The mice in the mentioned groups were euthanized with an anesthetic overdose of thiopental sodium (100 mg kg^{-1}) administered intraperitoneally. Blood samples were collected to analyze the creatine

Table 1 Animals used for SPION tests

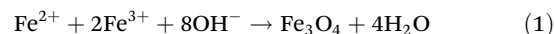|	C57BL/10		*mdx*	
Group	Identification	Quantity	Identification	Quantity
1	Sham	6	Sham	6
2	Magnet	6	Magnet	6
3	NPs	6	NPs	6
4	Magnet + NPs	6	Magnet + NPs	6
5	DFZ	6	DFZ	6
6	IBU	6	IBU	6
7	NPs + Magnet + DFZ	6	NPs + Magnet + DFZ	6
8	NPs + Magnet + IBU	6	NPs + Magnet + IBU	6

kinase (CK) protein by puncturing the caudal vena cava. In addition, liver and kidney toxicity studies were carried out with AST (aspartate aminotransferase), ALT (alanine aminotransferase), creatinine, and urea measurements.

2.3.5. Statistical analysis of data. We conducted a descriptive analysis using the statistical program Stata version 14.0 to validate the obtained data. We checked the quantitative variables for normality using the Shapiro–Wilk test. These variables were presented as measures of central tendency (mean and median) and variability values (standard deviation and 25th and 75th percentile values). We used the Student's *t*-test or the Mann–Whitney test to compare the groups, with a 95% confidence level.

3. Results and discussion

3.1. Synthesis of Fe$_3$O$_4$-(Cys)$_2$ by the co-precipitation method

One of the simplest and most effective chemical methods for producing magnetic nanoparticles, like iron oxides (Fe$_3$O$_4$ or γ-Fe$_2$O$_3$), is co-precipitation.[35] The industry values this technique for its scalability, reproducibility, and environmental friendliness.[35,36] In this methodology, Fe^{2+} and Fe^{3+} oxides are generated after the addition of a weak base, such as ammonium hydroxide, as described in the eqn (1):

$$Fe^{2+} + 2Fe^{3+} + 8OH^- \rightarrow Fe_3O_4 + 4H_2O \quad (1)$$

Previous studies have shown that L-cysteine can act as an efficient coating agent for SPIONs, enabling greater biocompatibility, antioxidant function, and water solubility, thus making them more suitable for biological applications.[20,30,37] Furthermore, the thiol group from L-Cys present on the surface of the NPs allows for the anchoring of drugs. This capability enables the development of a magnetically guided drug delivery system, which can transport the drug to the specific disease site within the body. In this study, we aimed to develop a system for targeted delivery of deflazacort and ibuprofen drugs to treat Duchenne muscular dystrophy, as shown in Fig. 2. Our goal is to reduce the severe side effects caused by these drugs when administered systemically. While there are existing studies on the use of SPIONs in cancer diagnosis and treatment, their use in treating muscular dystrophy has yet to be reported in the literature.

3.1.1. FTIR spectra. When comparing the spectra of L-Cys (magenta spectrum), Fe$_3$O$_4$-(Cys)$_2$ (red spectrum), and Fe$_3$O$_4$ (black spectrum) shown in Fig. 3, we observe the bands associated with the iron oxide core, present at 3447 cm^{-1} (νFe–OH) and 580 cm^{-1} (νFe–O).[38] Conversely, the same inference cannot be applied to the L-cysteine bands due to the presence of L-cystine (blue spectrum), a dimer formed by disulfide bridges resulting from the oxidation of the side-chain thiols.[39] Thus, the following bands observed in the Fe$_3$O$_4$-(Cys)$_2$ spectrum can be attributed to L-cystine: 3110 cm^{-1}, 2953 cm^{-1}, and 2920 cm^{-1}, which are attributed to the stretching of the –CH group; two characteristic bands at 1622 cm^{-1} and 1403 cm^{-1} associated with the asymmetric (ν_{assim} –COO$^-$) and symmetric (ν_{sim} –COO$^-$) stretching of the carboxylate group; and two
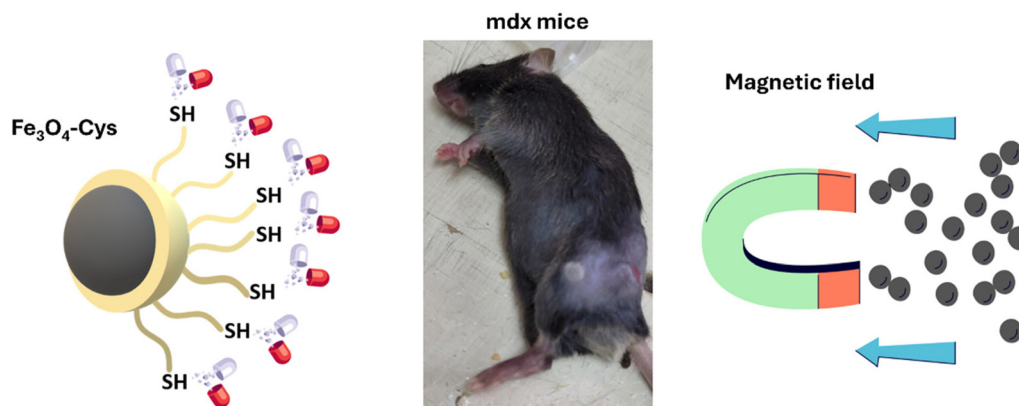
Fig. 2 Schematic representation of using Fe_3O_4-Cys for drug delivery in *in vivo* studies.

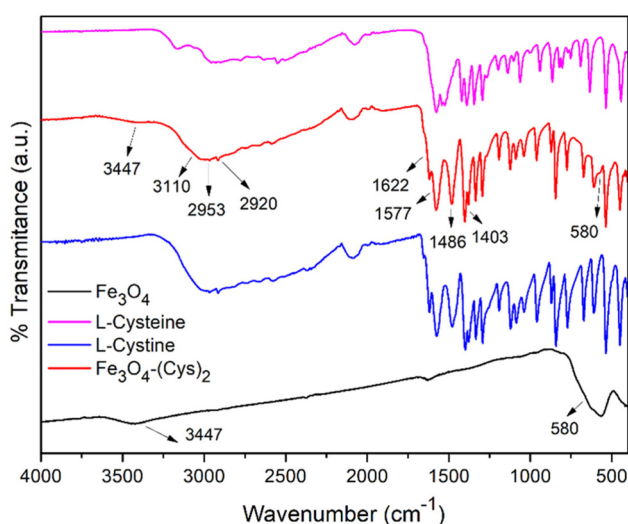**Fig. 3** FTIR spectra of Fe_3O_4 (black spectrum), Fe_3O_4-$(Cys)_2$ (red spectrum), L-cystine (blue spectrum), and L-cysteine (magenta spectrum).

bands at 1577 cm^{-1} and 1486 cm^{-1} referring to the angular deformation (δ N–H) and stretching (ν N–H) of the amino N–H bond.[30]

The anchoring of the drugs deflazacort (DFZ) and ibuprofen (IBU) to SPIONs functionalized with L-Cys is possible because the dimerization of cysteine only occurs in the solid state.[30] Thus, in aqueous media, as occurs during the anchoring process, we have the presence of cysteine and free thiol groups, allowing the drugs to bind. To confirm the dissociation of the disulfide group of L-cystine, returning to L-cysteine in dispersion, we quantified the thiol (SH) groups adsorbed on the surface of the SPIONs by reacting them with 5,5′-dithiobis-(2-nitrobenzoic acid) (DTNB, $C_{14}H_8N_2O_8S_2$, MM 396.3 g mol^{-1}). This compound contains a highly oxidative disulfide bond, which is stoichiometrically reduced by free thiol (–SH) groups through an exchange reaction, forming a mixed disulfide and releasing the TNB$^-$ anion.[40,41] We found a value of 0.10 mmol g^{-1} of SH in Fe_3O_4-Cys, a result that confirms the presence of free thiol groups in dispersion.

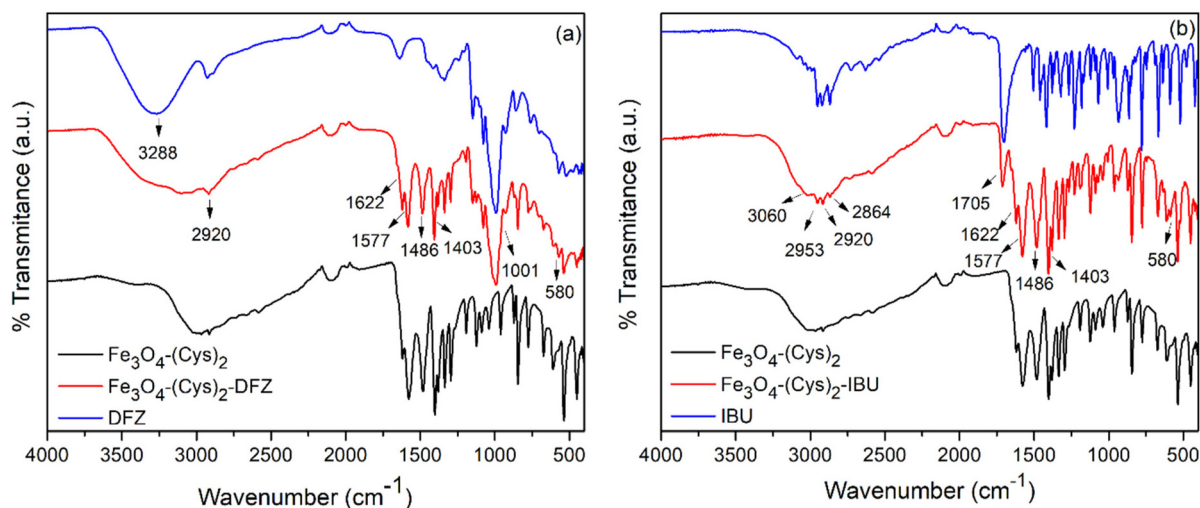**Fig. 4** (a) FTIR spectra of Fe_3O_4-$(Cys)_2$ (black line), Fe_3O_4-$(Cys)_2$-DFZ (blue line), and DFZ (red line) (b) FTIR spectra of Fe_3O_4-$(Cys)_2$ (black line), Fe_3O_4-$(Cys)_2$-IBU (blue line) and IBU (red line).

In the spectrum of Fe_3O_4-$(Cys)_2$-DFZ (red spectrum) shown in Fig. 4a, we can see the characteristic bands of L-cystine and deflazacort, demonstrating the dimerization of the cysteine into cystine and the anchoring of the drug to the system. The broad band located in the region near 3288 cm^{-1} is characteristic of the stretching vibration of the O–H bond (ν O–H) in the deflazacort molecule, and the intense band at 1001 cm^{-1} can
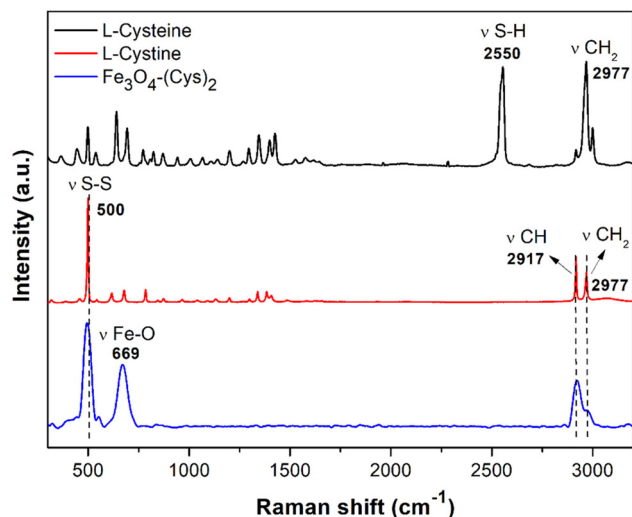

Fig. 5 Raman spectra of the standards L-cysteine (black spectrum) and L-cystine (red spectrum) and the Fe_3O_4-$(Cys)_2$ (blue spectrum), with the respective image of the sample analysis point.
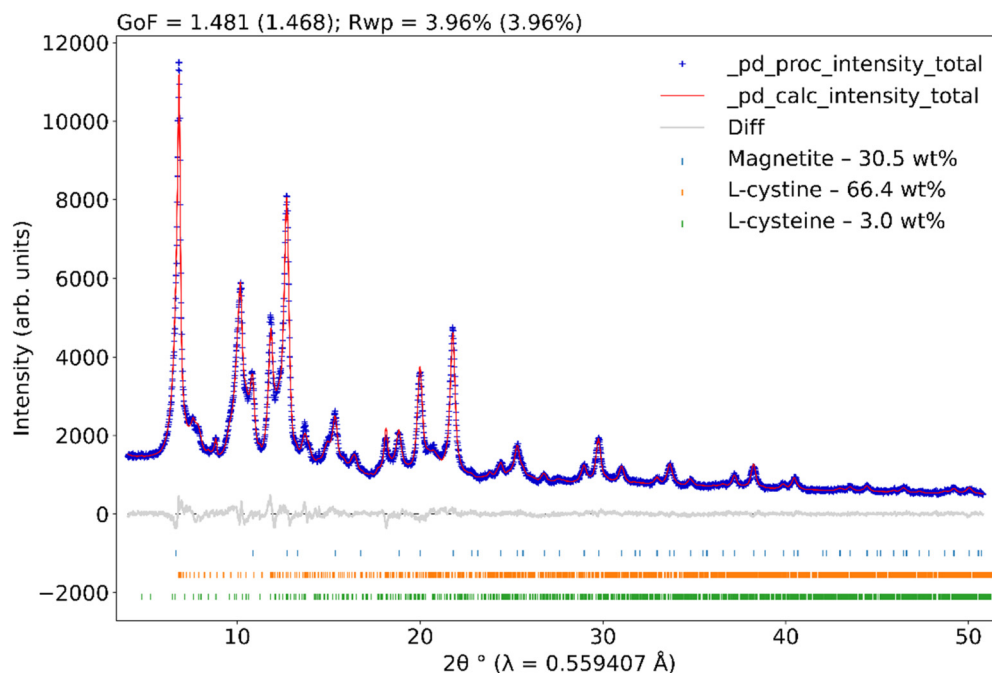
be attributed to the C–O–C stretching of the aromatic ring of the drug.[42] About the spectrum of the Fe_3O_4-$(Cys)_2$-IBU (red spectrum) shown in Fig. 4b, we can see the bands associated with L-cystine and the following bands referring to ibuprofen: a band characteristic of the stretching of the C=O bond at 1705 cm^{-1}, two bands at 2864 and 2920 cm^{-1} corresponding to the symmetrical and asymmetrical stretching of –CH$_2$, respectively, and a band between 3090–3018 cm^{-1} referring to the =C–H bond present in the benzene ring.[43] In addition, we observe a band associated with the Fe–O bond of the SPIONs (ν Fe–O) in 580 cm^{-1}.

With the confirmation of free thiol groups on the surface of the SPIONs, we believe that the interaction of L-cysteine with the nanoparticle surface occurs through the carboxylate and amino ion groups, which have free electrons in their structures, allowing them to bind to the metal surface through van der Waals interactions. Therefore, since no significant shifts in the bands associated with the –COO$^-$ and N–H groups were observed, we propose that their interaction with the nanoparticle surface occurs *via* physical adsorption.

3.1.2. Raman spectroscopy. Fig. 5 shows the Raman spectra of the L-cysteine, L-cystine, and Fe_3O_4-$(Cys)_2$. In the cysteine spectrum (black color), a band at 2550 cm^{-1} corresponds to the S–H bond of the thiol group, while a band at 2977 cm^{-1} indicates the –CH$_2$ stretching vibration. In the cystine spectrum (red color), a prominent band at 500 cm^{-1} is attributed to the stretching vibration of the S–S bond, accompanied by bands at 2917 cm^{-1} and 2977 cm^{-1} characteristic of the stretching vibrations of the –CH and –CH$_2$ bonds.[44]

Fig. 6 Rietveld plot for the Fe_3O_4-$(Cys)_2$ sample. The blue plus signs represents the observed pattern, while the red line indicates the calculated one. The gray line at the bottom of the figure represents the difference between the observed and calculated patterns. The vertical bars display the Bragg reflections of the magnetite (blue), L-cystine (orange), and L-cysteine (green) phases.
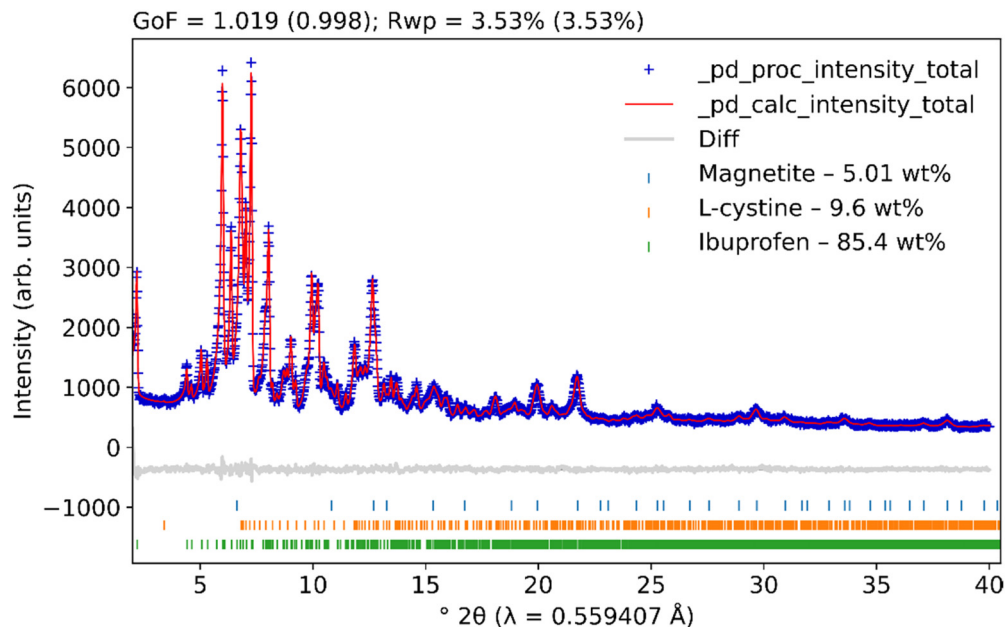
Fig. 7 Rietveld plot for the Fe_3O_4-Cys-IBU sample. The blue plus signs represents the observed pattern, while the red line indicates the calculated one. The gray line at the bottom of the figure represents the difference between the observed and calculated patterns. The vertical bars display the Bragg reflections of the magnetite (blue), L-cystine (orange), and ibuprofen (green) phases.

In the spectrum of Fe_3O_4-$(Cys)_2$, an intense band at 500 cm^{-1} confirms the presence of L-cystine in the synthesized system. The band at 669 cm^{-1} is attributed to the A_{1g} mode of the Fe–O bond vibration in magnetite,[45] while the bands at 2917 cm^{-1} and 2977 cm^{-1} indicate the vibrational modes of the –CH and –CH$_2$ bonds in the L-cystine structure.

3.1.3. Powder X-ray diffraction (PXRD). Rietveld plots of the Fe_3O_4-$(Cys)_2$ and Fe_3O_4-$(Cys)_2$-IBU were generated using the *pdCIFplotter* software.[46] The peak profiles were modeled considering the fundamental parameters approach[47] implemented in TOPAS-*Academic* V7 software.[48] We considered the crystal structures of Fe_3O_4, L-cysteine, L-cystine, and ibuprofen as described by Fleet,[49] Kolesov *et al.*,[50] Moggach *et al.*[51] and Freer *et al.*,[52] respectively. In Fig. 6, quantitative phase analysis (QPA) using PXRD patterns allowed us to infer the weight percentages of the magnetite (30.5(6) wt%), L-cystine (66.4(7) wt%), and L-cysteine (3.0(5) wt%) phases in the sample. We can infer that in the solid state, cysteine dimerizes into cystine through the oxidation of free thiol groups, a finding supported by FTIR and Raman Spectroscopy results. The calculated average crystallite size was (8.6(6)) nm. For the Fe_3O_4-$(Cys)_2$-IBU (Fig. 7), the determined weight percentages were as follows: magnetite (5.0(5) wt%), L-cystine (9.6(5) wt%), and ibuprofen (85.4(4) wt%). These values confirm the presence of ibuprofen in the sample, indicating a higher proportion of the drug relative to the other components. This excess of ibuprofen can be explained by the 1 : 5 mass ratio (Fe_3O_4-$(Cys)_2$: IBU) used during synthesis. Nonetheless, this did not compromise the effectiveness of the biological outcomes achieved with the Fe_3O_4-$(Cys)_2$-IBU system.

Fig. 8 shows the PXRD patterns of the Fe_3O_4, Fe_3O_4-$(Cys)_2$, Fe_3O_4-$(Cys)_2$-DFZ, and DFZ samples. Due to the low scattering power of atoms with a low atomic number (Z) when using a MoKα1 source, the data for the DFZ and Fe_3O_4-$(Cys)_2$-DFZ samples were obtained using a diffractometer equipped with a CuKα1 source. Therefore, to better visualize the PXRD patterns together, we used the Q vector ($Q = 4\pi \sin \theta/\lambda$) on the abscissa axis instead of the conventional 2θ angle. In the diffractogram of Fe_3O_4-$(Cys)_2$-DFZ (magenta line) peaks corresponding to the

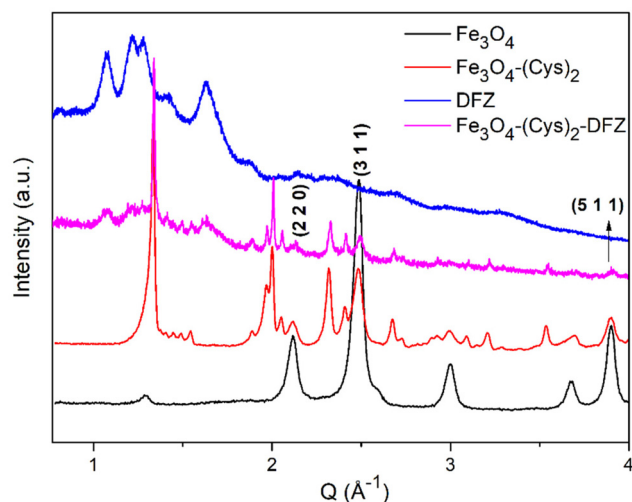**Fig. 8** X-ray powder diffraction patterns of Fe_3O_4 (black line), Fe_3O_4-$(Cys)_2$ (red line), Fe_3O_4-$(Cys)_2$-DFZ (magenta line) and DFZ (blue line). The diffractograms were normalized by the maximum peak intensity and vertically displaced for better visualization.

(2 2 0), (3 1 1), (5 1 1), and (4 4 0) planes of magnetite (JCPDS 19-0629) are observable, confirming the presence of SPIONs in the system. Furthermore, peaks related to the structure of deflazacort (blue line) and cystine (red line) are also evident, corroborating the successful attachment of the drug to the SPIONs functionalized with the biomolecule.

3.1.4. Transmission electron microscopy (TEM). Fig. 9a depicts the TEM image of some Fe_3O_4-$(Cys)_2$-DFZ nanoparticles. We can see that the nanoparticles exhibit an almost spherical shape; however, they show aggregation due to the presence of surface interactions from intermolecular forces. The size distribution histogram (Fig. 9b) revealed that the Fe_3O_4-$(Cys)_2$-DFZ system had an average diameter of 12.48 nm with a range of 6.40 to 19.60 nm. In the HR-TEM image (Fig. 9c), we confirmed the crystallinity of the nanoparticles by observing lattice planes, which are the result of electron inter-

action with atoms arranged in a crystalline lattice. We observed a d-spacing = 0.146 nm in the magnified area, characteristic of the (4 4 0) magnetite plane. The electron diffraction pattern (Fig. 9d) showed circular rings, confirming that the SPIONs are polycrystalline. The lattice spacings corresponding to each ring were calculated from the diffraction patterns and matched well with those of magnetite (JCPDS, no. 19-0629).[53] The intense glow of the electron rings and the matrix around the nanoparticles, indicated by the yellow arrow, is evidence of the presence of deflazacort in the synthesized system.

3.1.5. Magnetization measurements. An important characteristic of Fe_3O_4 nanoparticles for biomedical applications as drug carriers is their superparamagnetic behavior, which arises from forming magnetic monodomains. Fig. 10a shows the magnetization curves of Fe_3O_4 (black line), Fe_3O_4-$(Cys)_2$ (red line), and Fe_3O_4-$(Cys)_2$-DFZ (blue line), and Fig. 10b shows

Fig. 9 (a) TEM of Fe_3O_4-$(Cys)_2$-DFZ (b) Size distribution histogram of Fe_3O_4-$(Cys)_2$-DFZ (c) HR-TEM of Fe_3O_4-$(Cys)_2$-DFZ with emphasis on the region containing the (4 4 0) plane of magnetite (d) SAED (Selected Area Electron Diffraction) pattern of Fe_3O_4-$(Cys)_2$-DFZ.

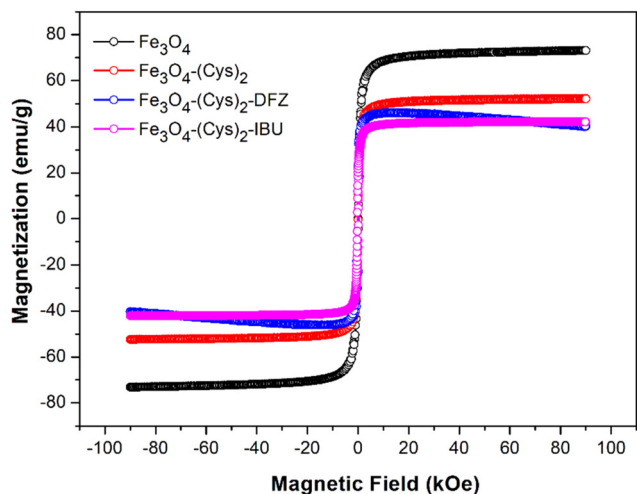**Fig. 10** Magnetization curves of (a) Fe_3O_4 (black line), Fe_3O_4-$(Cys)_2$ (red line) and Fe_3O_4-$(Cys)_2$-DFZ (blue line) (b) Fe_3O_4-$(Cys)_2$-IBU (magenta line).

the curve of Fe_3O_4-$(Cys)_2$-IBU (magenta line) obtained under isothermal magnetic conditions at room temperature. All the samples exhibited superparamagnetic behavior, displaying curves with negligible remanence and zero coercivity. The Fe_3O_4 NPs demonstrated saturation magnetization values of approximately 72 emu g^{-1}, a figure comparable to magnetite values found in previous research conducted by the group.[54,55] The Fe_3O_4-$(Cys)_2$, Fe_3O_4-$(Cys)_2$-DFZ, and Fe_3O_4-$(Cys)_2$-IBU samples showed saturation magnetization values of 52 emu g^{-1}, 40 emu g^{-1}, and 42 emu g^{-1}, respectively. It is important to emphasize that the saturation was measured as a function of the Fe_3O_4 mass. The decrease in magnetization may be due to the layer of organic material around the nanoparticle, being even more pronounced in the samples with the drugs anchored to the surface (greater amount of organic material). Organic molecules exhibit diamagnetic properties, which trigger a reduction in response to the applied external magnetic field. Additionally, contributions from intrinsic particles and shape and stress anisotropies due to different ligands may further contribute to the decrease in magnetization.[56]

An ideal saturation magnetization range for magnetic nanoparticles in drug delivery applications is typically between 30 and 50 emu g^{-1}. This range provides sufficient magnetic responsiveness for precise manipulation and effective targeting, essential for controlled and targeted drug delivery.[57,58] These results suggest that the synthesized nanoparticles possess sufficient magnetic strength for these applications.

3.1.6. Hydrodynamic size and zeta potential. The hydrodynamic size of the Fe_3O_4-$(Cys)_2$ sample was measured to be approximately 119.3 ± 4.9 nm, with a low polydispersity index (PDI) of about 0.19 ± 0.07, indicating a uniform size distribution. The size measured here is larger than the data obtained from X-ray diffractometry and transmission electron microscopy due to the presence of water molecules around the

nanoparticles (solvation), solvated ions, and aggregations arising from strong, attractive interactions, such as van der Waals forces, depletion forces, and hydrophobic interactions.[59–61] The zeta potential was approximately −23.7 ± 3.3 mV, indicating good colloidal stability and surface charges on the nanoparticles. These surface charges create repulsion between the nanoparticles, resulting in stable, monodisperse systems with fewer aggregates.

According to the results in Table 2, both systems, Fe_3O_4-$(Cys)_2$-DFZ and Fe_3O_4-$(Cys)_2$-IBU, showed acceptable hydrodynamic diameter values, 159 ± 21 nm and 188 ± 29 nm, respectively. This increase in size (from 119 ± 5 nm to 159 ± 21 nm and 188 ± 29 nm) is associated with the addition of new molecules to the system due to the anchoring of the drugs to the Fe_3O_4-$(Cys)_2$. PDI values increased from 0.19 ± 0.07 associated with Cys-SPIONs to 0.29 ± 0.05 and 0.24 ± 0.09 associated with Fe_3O_4-$(Cys)_2$-DFZ and Fe_3O_4-$(Cys)_2$-IBU, respectively. Finally, about zeta potential values, we can observe an increase for both samples, Fe_3O_4-$(Cys)_2$-DFZ (−24.2 ± 3.3) and Fe_3O_4-$(Cys)_2$-IBU (−25.6 ± 4.2). This shows a greater number of negative charges on the surface of the nanoparticles due to the presence of the added drugs, which allows for greater repulsion between them and better colloidal dispersion, which is extremely important for subsequent biomedical applications.

4. Biological assays

After 7 days of implanting the magnet in the animal's quadriceps and injecting nanoparticles, blood samples were taken for biochemical analysis. These tests were conducted to assess the toxicity of the applied systems by monitoring the levels of liver enzymes (ALTL – alanine aminotransferase and ASTL – aspartate aminotransferase), creatinine and urea (renal assessment), and creatine kinase (CK – muscle marker).

4.1. Liver enzymes

Fig. 11 presents the graphs depicting the liver enzyme levels of ALTL (Fig. 11a) and ASTL (Fig. 11b) for the 16 treatment groups. These groups include both healthy mice (black) and mice with Duchenne Muscular Dystrophy (*mdx*). Statistical interactions between groups were evaluated using Student's *t*-test at a 95% confidence level ($p < 0.005$).

In *mdx* mice, the levels associated with the ALTL and ASTL enzymes are already altered due to the generalized muscle inflammation present in the body,[62] as we can see in both

Table 2 Scattering characterization data of synthesized systems. R_H stands for the hydrodynamic radius, μ_2/Γ^2 is the polydispersity index, and ζ is the zeta potential of the nanoparticles

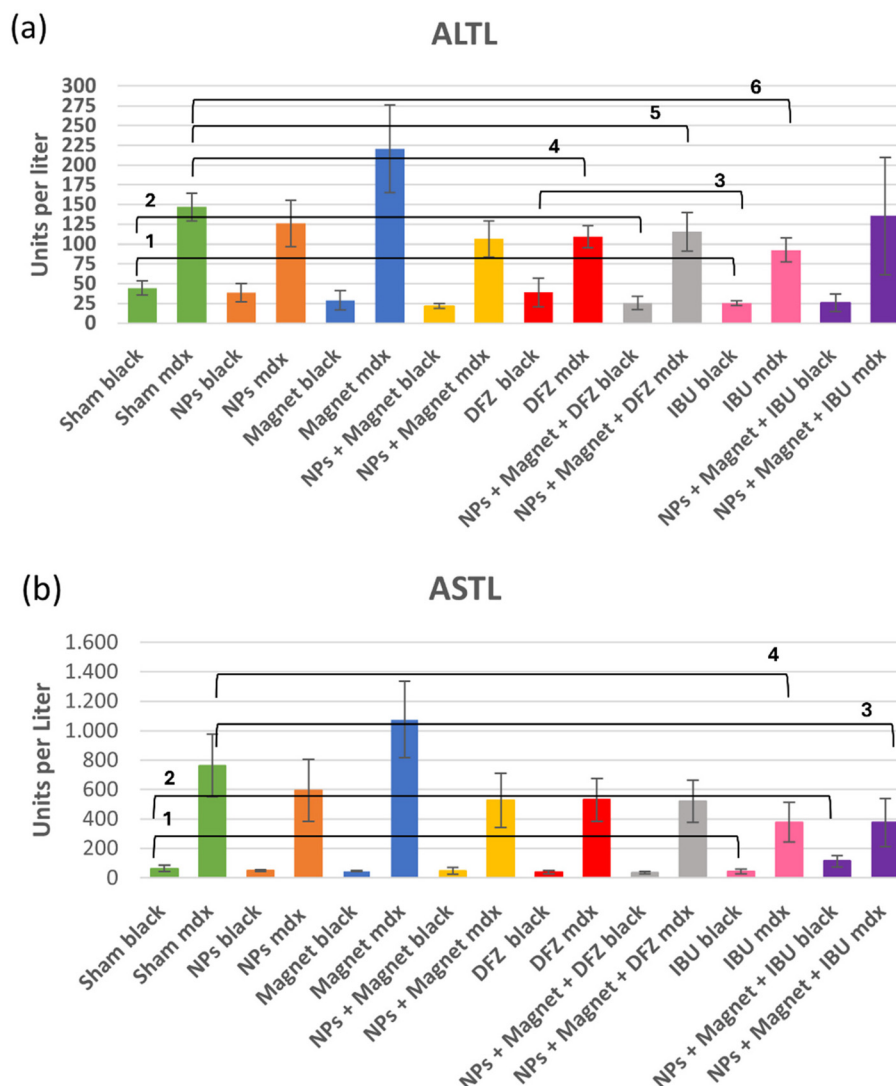| Sample	R_H (nm)	μ_2/Γ^2	ζ (mV)
Fe_3O_4-$(Cys)_2$	119.3 ± 4.9	0.190 ± 0.07	−23.7 ± 3.3
Fe_3O_4-$(Cys)_2$-DFZ	159 ± 21	0.291 ± 0.049	−24.2 ± 3.3
Fe_3O_4-$(Cys)_2$-IBU	188 ± 29	0.244 ± 0.087	−25.6 ± 4.2

View Article Online

Fig. 11 Graphs obtained from the analysis of biochemical tests on healthy and dystrophic mice demonstrate the quantification of the enzymes (a) ALTL (1 p = 0.0027, 2 p = 0.0104, 3 p = 0.0303, 4 p = 0.0030, 5 p = 0.0281, 6 p = 0.0012) and (b) ASTL (1 p = 0.0374, 2 p = 0.0176, 3 p = 0.0067, 4 p = 0.0038) with their respective standard deviations and statistical interactions.

graphs in the Sham *mdx* group (column represented by green). Only with the treatment based on the administration of saline solution could higher levels of these enzymes be seen in the Sham *mdx* group compared to the Sham black group.

Concerning the black mice, a decrease in the ALTL enzyme (Fig. 11a) was observed in the IBU black group compared to the Sham black group (interaction 1, p = 0.0027), in the NPs + Magnet + DFZ black group compared to the Sham black group (interaction 2, p = 0.0104) and between the DFZ black and IBU black groups (interaction 3, p = 0.0303), showing that among the black groups, treatment with Ibuprofen proved to be more effective in reducing the liver enzyme ALTL.

Significant interactions in the groups involving *mdx* mice demonstrated a decrease in the liver enzyme ALTL. Compared to the Sham *mdx* group, the DFZ *mdx* (interaction 4, p = 0.0030), NPs + Magnet + DFZ *mdx* (interaction 5, p = 0.0281),

and IBU *mdx* (interaction 6, p = 0.0012) groups showed the most significant reductions, with the greatest decrease observed in the IBU *mdx* group.

Regarding the ASTL enzyme (Fig. 11b), a decrease was also observed in both groups (black and *mdx*), especially with the treatment involving the administration of the drug ibuprofen. In the black mice, this decrease was evident in the interactions between the Sham black group and the IBU black group (interaction 1, p = 0.0374) and the NPs + Magnet + IBU black group (interaction 2, p = 0.0176). For the dystrophic mice, the interactions were observed between the Sham *mdx* and IBU *mdx* groups (interaction 3, p = 0.0067) and the Sham *mdx* and NPs + Magnet + IBU *mdx* groups (interaction 4, p = 0.0038).

The results showed no increase in liver enzymes after 7 days of treatment. On the contrary, a decrease was noted, suggesting the absence of hepatotoxicity[63] resulting from the

administration of nanoparticles and the drugs Deflazacort and Ibuprofen in both healthy and dystrophic mice.

4.2. Kidney enzymes

The graphs in Fig. 12 present the levels of the enzyme creatinine (Fig. 12a) and the metabolite urea (Fig. 12b) obtained from biochemical tests of the 16 treatment groups, which include both healthy mice (black) and dystrophic mice (mdx). Statistical evaluation of interactions between the groups was performed using Student's t-test, with significant differences at a p-value < 0.05 and a confidence level of 95%.

In both the black and mdx mice groups, an increase in creatinine levels was observed after treatment with deflazacort and ibuprofen anchored in nanoparticles. Significant interactions were noted in black mice between the Sham black and NPs + Magnet + DFZ black groups (interaction 1, $p = 0.0330$) and in mdx mice between the Sham mdx and NPs + Magnet + IBU mdx groups (interaction 2, $p = 0.0102$). Administration of corticosteroids and anti-inflammatories typically results in reduced renal blood flow, sodium retention, and water retention in the body, leading to decreased renal function and elevated creatinine levels.[64] Furthermore, a significant interaction was observed in mdx mice between the Sham mdx and NPs + Magnet mdx groups (interaction 3, $p = 0.0412$), showing increased creatinine levels following treatment with nanoparticles and a magnet. However, this increase remains within
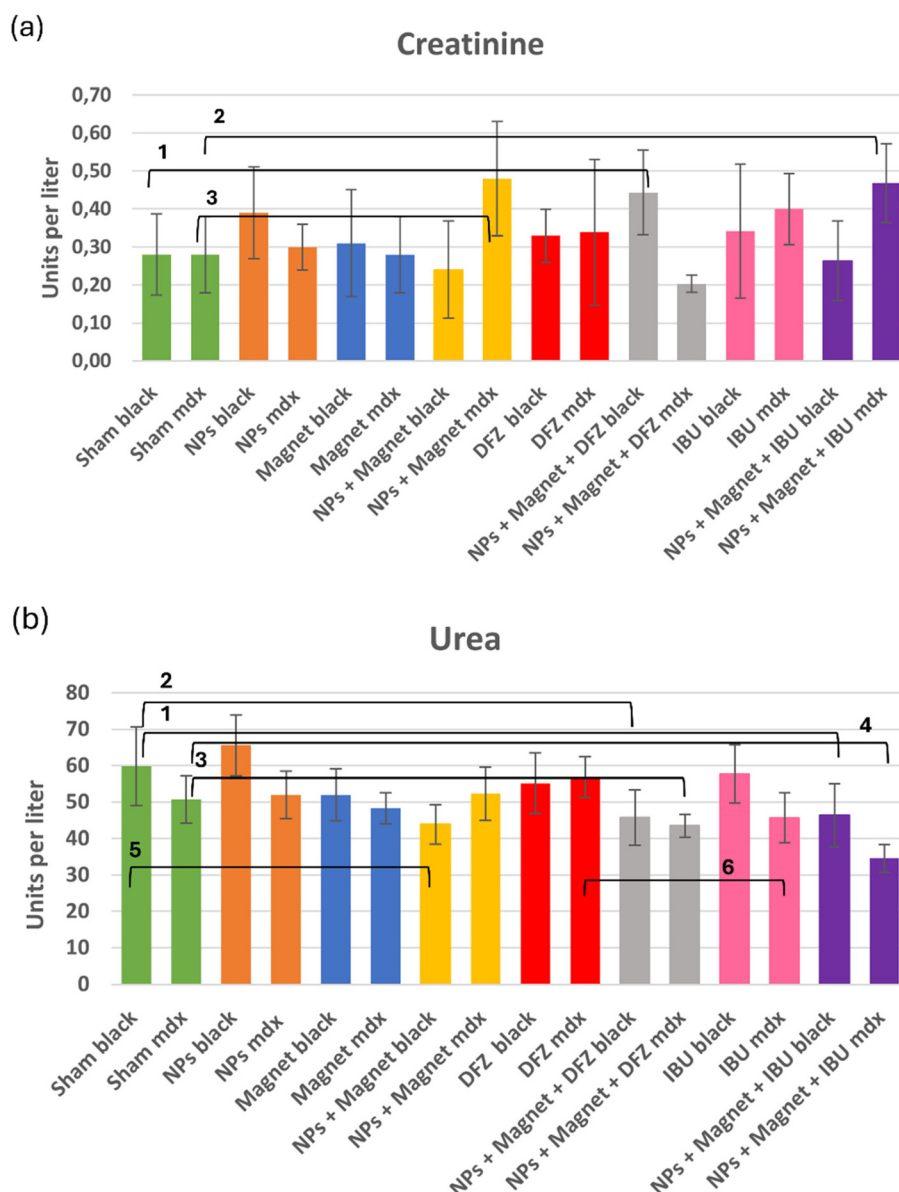

Fig. 12 Graphs obtained from the analysis of biochemical exams of healthy and dystrophic mice demonstrating the quantification of (a) creatinine (1 $p = 0.0330$, 2 $p = 0.0102$, 3 $p = 0.0412$) and (b) urea (1 $p = 0.0434$, 2 $p = 0.0216$, 3 $p = 0.0275$, 4 $p = 0.0004$, 5 $p = 0.0051$, 6 $p = 0.0055$) with their respective standard deviations and statistical interactions.

the normal range. Data from a group (not yet published, $n = 52$) showed that creatinine levels can vary from 0.1 to 0.65 units per liter in control animals. Therefore, while creatinine increased in the treated animals, their levels are still within the normal range, demonstrating that the applied doses are safe.

Despite this conclusion, increased iron interferes with hematopoiesis, alters the relationship of components of the solid phase of peripheral blood, and potentially interferes with ultrafiltration. Metabolically, iron decreases renal excretion and, depending on the dose, may interfere with creatinine levels in animals treated with nanocomposites.

Furthermore, ferroptosis has already been reported in the literature[65] as a form of cell death resulting from iron accumulation. This condition is characterized by the lethal buildup of lipid peroxidation products catalyzed by iron ions and could occur in the treatment in question. To avoid cellular damage, we analyzed creatinine levels. Although a difference was observed, renal damage caused by the treatment was not characterized.

Regarding the urea metabolite (Fig. 12b), black and *mdx* mice exhibited decreased levels following treatment with drug-conjugated nanoparticles. In black mice, interactions between the Sham black group and the NPs + Magnet + DFZ black group (interaction 1, $p = 0.0434$) and NPs + Magnet + IBU black group (interaction 2, $p = 0.0216$) indicated an impact on renal activity potentially linked to drug administration. Similarly, in *mdx* mice, interactions between the Sham *mdx* group and the NPs + Magnet + DFZ *mdx* group (interaction 3, $p = 0.0275$) and NPs + Magnet + IBU *mdx* group (interaction 4, $p = 0.0004$) demonstrated a reduction in urea levels.

In future studies, these results will be compared with data obtained from histological and molecular analyses (PCR) to verify the effects caused by the administration of the drugs

individually and to confirm the non-toxicity of the synthesized system, corroborating with the results obtained in analysis section 4.1.

4.3. Muscle marker creatine kinase (CK)

The CK value is highly elevated in patients with Duchenne Muscular Dystrophy, about 2000 times higher than the upper limit of normality (Reference Values = 26 to 189 U L^{-1}).[66] In Fig. 13, we have a graph with the values of the CK enzyme in the Sham black control animal and in dystrophic animals subjected to different types of treatments:

The graph shows that the treated groups demonstrated improvement compared to the Sham *mdx* control group, indicating a reduction in CK enzyme levels, notably in the NPs + Magnet + DFZ *mdx* group. However, the CK levels in the dystrophic mice analyzed in this study (6 animals per group) exhibited significant variability, resulting in a notably large standard deviation, particularly within the control group. As a result, despite employing statistical analysis using the Student's *t*-test, we did not observe significant differences with a *p*-value < 0.05 between the control and treated groups due to the substantial sample variability. This variability in creatine kinase enzyme levels in the *mdx* mice is likely caused by fluctuations in physical activity and periodic episodes of muscle degeneration and regeneration. When the mice are more active or subjected to higher physical stress, muscle tissue damage increases, leading to higher CK levels in the plasma. Therefore, the physiological condition of the mouse at the time of sample collection can significantly influence the data obtained, serving as the main factor contributing to the observed variability.[67,68]

Upon examining the data provided by The Jackson Laboratory,[69] which is the source of the mdx strain used, we found that their reported CK levels are like ours, also showing
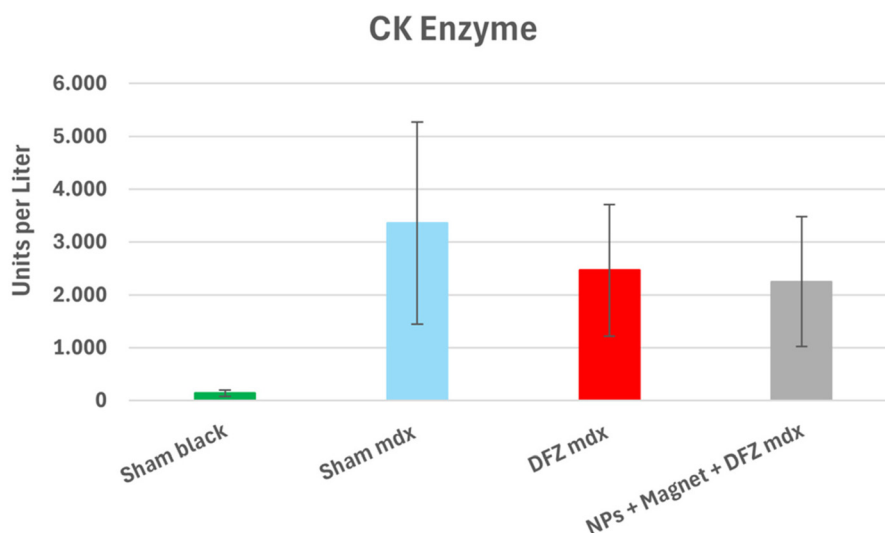
Fig. 13 Graph obtained from the analysis of biochemical exams of healthy and dystrophic mice demonstrating the quantification of the enzyme Creatine Kinase (CK) with their respective standard deviations.

a degree of variation. Additional factors, such as sample collection methods and the analytical phase, can contribute to hemolysis, which may affect these parameters. During our collections, we took precautions to minimize any damage.

Another important factor is the substantial reduction in CK variability in animals treated with Deflazacort (Fig. 13), which reduces inflammation and stabilizes CK levels in treated animals compared to the Sham *mdx* group. This effect is one of the reasons for its use in clinical practice[70] and why it was chosen for this treatment.

Thus, the use of the synthesized drug delivery system enables targeted delivery of the drug to the disease site (quadriceps region, where the magnet was inserted), reducing the side effects associated with the conventional administration of deflazacort and ibuprofen. Furthermore, the slight decrease observed in the NPs + Magnet + DFZ mdx group, compared to the DFZ mdx group, is promising given the short treatment period used in mice (7 days), considering that individuals with Duchenne muscular dystrophy require lifelong treatment with these drugs. In future studies, we intend to extend the treatment duration to 21 days to enhance the results. Further, *in vivo* gene expression studies will be conducted to evaluate the treatment's efficacy at the molecular level.

5. Conclusions

The coprecipitation method was employed to synthesize Superparamagnetic Iron Oxide Nanoparticles, resulting in magnetite nanoparticles with a nearly spherical shape and a size of approximately 10 nm in the solid state, as confirmed by TEM and PXRD techniques. FTIR analysis verified the effective surface functionalization of SPIONs and the attachment of drugs to thiol groups of biomolecules. The SPIONs demonstrated superparamagnetic behavior, indicating the formation of nanoparticles with magnetic monodomains, and exhibited a hydrodynamic size of approximately 120 nm with a Polydispersity Index of 0.200, suitable for biological applications in aqueous environments. In biological studies, quantification of liver enzymes ALTL and ASTL confirmed the non-hepatotoxicity of Fe_3O_4-$(Cys)_2$-DFZ and Fe_3O_4-$(Cys)_2$-IBU systems. At the same time, measurement of renal markers creatinine and urea showed no evidence of kidney damage. Promising results were also observed for the CK enzyme, indicating an improvement trend in inflammation caused by DMD, thereby confirming the effective targeting of nanoparticles without interfering with ferric homeostasis.

Author contributions

Only the authors listed in the authorship of the article contributed to the writing of this paper. MLS: writing – original draft, methodology, investigation, conceptualization, writing – review & editing. TNB: methodology. FLAF: methodology, funding acquisition. FFF: software, formal analysis, writing – review &

editing. DF: resources, conceptualization. PF, GP: methodology, data curation, conceptualization, resources. PSH: investigation, writing – review & editing, conceptualization, project administration, supervision, funding acquisition, resources.

Data availability

Data will be available upon request.

Conflicts of interest

There are no conflicts to declare.

Acknowledgements

References

1 N. Datta and P. S. Ghosh, *Curr. Neurol. Neurosci. Rep.*, 2020, **20**, 14–26, DOI: **10.1007/s11910-020-01034-6**.

2 F. Leigh, A. Ferlini, D. Biggar, K. Bushby, R. Finkel, L. P. Morgenroth and K. R. Wagner, *Pediatrics*, 2018, **142**, S5–S16, DOI: **10.1542/peds.2018-0333C**.

3 D. J. Birnkrant, K. Bushby, C. M. Bann, S. D. Apkon, A. Blackwell, D. Brumbaugh, L. E. Case, P. R. Clemens, S. Hadjiyannakis, S. Pandya, N. Street, J. Tomezsko, K. R. Wagner and L. M. Ward, *Lancet Neurol.*, 2018, **17**, 251–267, DOI: **10.1016/S1474-4422(18)30024-3**.

4 Y. Shimizu-Motohashi, T. Murakami, E. Kimura, H. Komaki and N. Watanabe, *Orphanet J. Rare Dis.*, 2018, **13**, 93–106, DOI: **10.1186/s13023-018-0834-2**.

5 M. Okubo, S. Noguchi, S. Hayashi, H. Nakamura, H. Komaki, M. Matsuo and I. Nishino, *Hum. Genet.*, 2020, **139**, 247–255, DOI: **10.1002/humu.22758**.

6 Y. Shimizu-Motohashi, H. Komaki, N. Motohashi, S. Takeda and T. Yokota, *J. Pers. Med.*, 2019, **9**, 1–14, DOI: **10.3390/jpm9010001**.

7 R. Korinthenberg, *Dev. Med. Child Neurol.*, 2018, **61**, 292–297, DOI: **10.1111/dmcn.14129**.

8 D. Duan, *Molecular Therapy*, 2018, **26**, 1–20, DOI: **10.1016/j.ymthe.2018.07.011**.

9 I. E. C. Verhaart, *Nat. Rev. Neurol.*, 2019, **15**, 373–386, DOI: **10.1038/s41582-019-0203-3**.

10 Y. Zhang, T. Nishiyama, E. N. Olson and R. Bassel-Duby, *Exp. Cell Res.*, 2021, **408**(1), 112844–112853, DOI: **10.1016/j.yexcr.2021.112844**.

11 K. Reczyńska, M. Marszałek, A. Zarzycki, W. Reczyński, K. Kornaus, E. Pamuła and W. Chrzanowski, *Nanomaterials*, 2020, **10**, 1076–1102, DOI: **10.3390/nano10061076**.

12 A. M. M. Dias, A. Courteau, P. S. Bellaye, E. Kohli, A. Oudot, P. E. Doulain, C. Petitot, P. M. Walker, R. Decréau and P. Collin, *Pharmaceutics*, 2022, **14**, 2388–2424, DOI: **10.3390/pharmaceutics14112388**.

13 M. Pourmadadi, E. Rahmani, A. Shamsabadipour, S. Mahtabian, M. Ahmadi, A. Rahdar and A. M. Díez-Pascual, *Nanomaterials*, 2022, **12**, 3873–3902, DOI: **10.3390/nano12213873**.

14 N. Tyagi, P. Gupta, Z. Khan, Y. R. Neupane, B. Mangla, N. Mehra, T. Ralli, A. Alhalmi, A. Ali, O. Al Kamaly, A. Saleh, F. A. Nasr and K. Kohli, *Molecules*, 2023, **28**, 2343–2363, DOI: **10.3390/molecules28052343**.

15 S. Palanisamy and Y. M. Wang, *Dalton Trans.*, 2019, **48**, 9490–9515, DOI: **10.1039/c9dt00459a**.

16 S. D. Oberdick, K. V. Jordanova, J. T. Lundstrom, G. Parigi, M. E. Poorman, G. Zabow and K. E. Keenan, *Sci. Rep.*, 2023, **13**, 11520–11533, DOI: **10.1038/s41598-023-38222-6**.

17 P. D. Sruthi, C. S. Sahithya, C. Justin, C. SaiPriya, K. S. Bhavya, P. Senthilkumar and A. V. Samrot, *J. Cluster Sci.*, 2019, **30**, 11–24, DOI: **10.1016/j.crgsc.2021.100066**.

18 S. M. Dadfar, D. Camozzi, M. Darguzyte, K. Roemhild, P. Varvarà, J. Metselaar, S. Banala, M. Straub, N. Güvener, U. Engelmann, I. Slabu, M. Buhl, J. Van Leusen, P. Kögerler, B. Hermanns-Sachweh, V. Schulz, F. Kiessling and T. Lammers, *J. Nanobiotechnol.*, 2020, **18**, 22–35, DOI: **10.1186/s12951-020-0580-1**.

19 G. N. A. Rego, M. P. Nucci, J. B. Mamani, F. A. Oliveira, L. C. Marti, I. S. Filgueiras, J. M. Ferreira, C. C. Real, D. de P. Faria, P. L. Espinha, D. M. C. Fantacini, L. E. B. Souza, D. T. Covas, C. A. Buchpiguel and L. F. Gamarra, *Int. J. Mol. Sci.*, 2020, **21**, 958–989, DOI: **10.3390/ijms21030958**.

20 J. M. Beltrame, B. B. P. Ribeiro, C. Guindani, G. Candiotto, K. B. Felipe, R. Lucas, A. D. Zottis, E. Isoppo, C. Sayer and P. H. H. de Araújo, *Pharmaceutics*, 2023, **15**, 1000–1015, DOI: **10.3390/pharmaceutics15031000**.

21 H. Nazari, A. Heirani-Tabasi, M. Hajiabbas, M. Salimi Bani, M. Nazari, V. Pirhajati Mahabadi, I. Rad, M. Kehtari, S. H. Ahmadi Tafti and M. Soleimani, *J. Cell. Biochem.*, 2020, **121**, 2981–2993, DOI: **10.3390/pharmaceutics12070604**.

22 A. A. Abd Elrahman and, *Mansour.* Journal of Drug Delivery Science and Technology, 2019, **52**, 702–712, DOI: **10.1016/j.jddst.2019.05.030**.

23 E. Allard-Vannier, S. Cohen-Jonathan, J. Gautier, K. Hervé-Aubert, E. Munnier, M. Soucé, P. Legras, C. Passirani and I. Chourpa, *Eur. J. Pharm. Biopharm.*, 2012, **81**, 498–505, DOI: **10.1016/j.ejpb.2012.04.002**.

24 Y. Meng, S. Han, Z. Gu and J. Wu, *Adv. Ther.*, 2020, **3**, 1900142–1900155, DOI: **10.1002/adtp.201900142**.

25 A. Bhattacharyya, E. Stavitski, J. Dvorak and C. E. Martínez, *Geochim. Cosmochim. Acta*, 2013, **122**, 89–100, DOI: **10.1016/j.gca.2013.08.012**.

26 L. Abarca-Cabrera, P. Fraga-García and S. Berensmeier, *Biomater. Res.*, 2021, **25**, 12–30, DOI: **10.1186/s40824-021-00212-y**.

27 A. P. Vieira, G. Berndt, I. G. De Souza Junior, E. Di Mauro, A. Paesano, H. De Santana, A. C. S. Da Costa, C. T. B. V. Zaia and D. A. M. Zaia, *Amino Acids*, 2011, **40**, 205–214, DOI: **10.1007/s00726-010-0635-y**.

28 C. Soler-Alfonso, N. Pillai, E. Cooney, K. R. Mysore, S. Boyer and F. Scaglia, *Mol. Genet. Metab. Rep.*, 2019, **19**, 100453–100457, DOI: **10.1016/j.ymgmr.2019.100453**.

29 T. Britos, N. Santana, M. L. Schumacher, E. Barbosa, A. de Espindola, C. Chagas, F. L. A. Fonseca, F. F. Ferreira and P. S. Haddad, *Next Nanotechnol.*, 2024, **6**, 100076–100084, DOI: **10.1016/j.nxnano.2024.100076**.

30 T. N. Britos, C. E. Castro, B. M. Bertassoli, G. Petri, F. L. A. Fonseca, F. F. Ferreira and P. S. Haddad, *Mater. Sci. Eng., C*, 2019, **99**, 171–179, DOI: **10.1016/j.msec.2019.01.118**.

31 B. Odintsov, J. L. Chun, J. A. Mulligan and S. E. Berry, *Magn. Reson. Med.*, 2011, **66**, 1704–1714, DOI: **10.1186/scrt191**.

32 K. S. Cahill, G. Gaidosh, J. Huard, X. Silver, B. J. Byrne and G. A. Walter, *Transplantation*, 2004, **78**, 1626–1633, DOI: **10.1016/j.nurt.2007.05.010**.

33 G. A. Walter, K. S. Cahill, J. Huard, H. Feng, T. Douglas, H. L. Sweeney and J. W. M. Bulte, *Magn. Reson. Med.*, 2004, **51**, 273–277, DOI: **10.1007/978-0-387-72027-2_6**.

34 M. M. Molina, A. B. Seabra, M. G. De Oliveira, R. Itri and P. S. Haddad, *Mater. Sci. Eng., C*, 2013, **33**, 746–751, DOI: **10.1016/j.msec.2012.10.027**.

35 S. Laurent, D. Forge, M. Port, A. Roch, C. Robic, L. Vander Elst and R. N. Muller, *Chem. Rev.*, 2008, **108**, 2064–2110, DOI: **10.1021/cr068445e**.

36 A. H. Lu, E. L. Salabas and F. Schüth, *Angew. Chem. Int. Ed.*, 2007, **46**, 1222–1244, DOI: **10.1002/anie.200602866**.

37 J. M. Betrane, B. B. P. Ribeiro, C. Guindani, C. Graziâni, K. B. Felipe, R. Lucas, A. D. A. Zottis, E. Isoppo, C. Sayer and P. H. H. Araújo, *Phamaceutics*, 2023, **15**, 1000–10015, DOI: **10.3390/pharmaceutics15031000**.

38 E. K. U. Larsen, T. Nielsen, T. Wittenborn, H. Birkedal, T. Vorup-Jensen, M. H. Jakobsen, L. Ostergaard, M. R. Horsman, F. Besenbacher, K. A. Howard and J. Kjems, *ACS Nano*, 2009, **3**, 1947–1951, DOI: **10.1021/nn900330m**.

39 P. A. Fernandes and M. J. Ramos, *Chem. – Eur. J.*, 2004, **10**, 257–266, DOI: **10.1002/chem.200305343**.

40 P. W. Riddles, R. L. Blakeley and B. Zerner, *Methods Enzymol.*, 1983, **91**, 49–60, DOI: **10.1016/S0076-6879(83)91010-8**.

41 J. R. Winther and C. Thorpe, *Biochim. Biophys. Acta*, 2014, **1840**, 838–846, DOI: **10.1016/j.bbagen.2013.03.031**.

42 O. Kumar, A. Prameela Rani and V. Saikishore, *Res. J. Pharm., Biol. Chem. Sci.*, 2014, **5**, 211.

43 P. K. Le Kien Anh Le, *J. Chem. Eng. Process Technol.*, 2015, **6**, 2–6, DOI: **10.4172/2157-7048.1000220**.

44 Y. Su, E. Hessou, E. Colombo, G. Belletti, A. Moussadik, I. T. Lucas, V. Frochot, M. Daudon, S. Rouzière and D. Bazin, *Amino Acids*, 2022, 1123–1133, DOI: **10.1007/s00726-022-03144-6**.

45 A. M. Jubb and H. C. Allen, *ACS Appl. Mater. Interfaces*, 2010, **2**, 2804–2812, DOI: **10.1021/am1004943**.

46 M. R. Rowles, *J. Appl. Crystallogr.*, 2022, **55**, 631–637, DOI: **10.1107/S1600576722003478**.

47 R. W. Cheary, A. A. Coelho and P. P. Cline, *J. Res. Natl. Inst. Stand. Technol.*, 2004, **109**, 1–25, DOI: **10.6028/jres.109.002**.

48 A. A. Coelho, *J. Appl. Crystallogr.*, 2018, **51**, 210–218, DOI: **10.1107/S1600576718000183**.

49 M. E. Fleet, *Acta Crystallogr., Sect. B*, 1981, **37**, 917–920, DOI: **10.1107/S0567740881004597**.

50 B. A. Kolesov, V. S. Minkov, E. V. Boldyreva and T. N. Drebushchak, *J. Phys. Chem. B*, 2008, **112**, 12827–12839, DOI: **10.1021/jp804142c**.

51 S. A. Moggach, D. R. Allan, S. Parsons, L. Sawyer and J. E. Warren, *J. Synchrotron Radiat.*, 2005, **12**, 598–607, DOI: **10.1107/S0909049505019850**.

52 S. D. B. Freer, *Acta Crystallogr., Sect. C: Cryst. Struct. Commun.*, 1993, **49**, 1378–1380, DOI: **10.1107/S0108270193000629**.

53 A. Ozdemir, M. S. Ekiz, A. Dilli, M. O. Guler and A. B. Tekinay, *RSC Adv.*, 2016, **6**, 45135–45146, DOI: **10.1039/C6RA07380H**.

54 G. F. L. Pereira, F. N. Costa, J. A. Souza, P. S. Haddad and F. F. Ferreira, *J. Magn. Magn. Mater.*, 2018, **456**, 108–117, DOI: **10.1016/j.jmmm.2018.02.020**.

55 P. S. Haddad, E. L. Duarte, M. S. Baptista, G. F. Goya, C. A. P. Leite and R. Itri, *Progress in Colloid and Polymer Science*, 2004, **128**, 232–238, DOI: **10.1007/b97092**.

56 I. Campos, A. Espindola, C. Chagas, E. Barbosa, C. E. Castro, C. Molina, F. L. A. Fonseca and P. S. Haddad, *SN Appl. Sci.*, 2020, **2**, 456–468, DOI: **10.1007/s42452-020-2265-7**.

57 Y. Hadadian, H. Masoomi, A. Dinari, C. Ryu, S. Hwang, S. Kim, B. K. Cho, J. Y. Lee and J. Yoon, *ACS Omega*, 2022, **7**, 15996–16012, DOI: **10.1021/acsomega.2c01136**.

58 J. Estelrich, E. Escribano, J. Queralt and M. A. Busquets, *Int. J. Mol. Sci.*, 2015, **16**, 8070–8101, DOI: **10.3390/ijms16048070**.

59 J. Goodwin, *Colloids and Interfaces with Surfactants and Polymers*, 2nd edn, 2009.

60 P. C. De Sousa Filho and O. A. Serra, *Química Nova*, 2015, **38**, 679–696, DOI: **10.5935/0100-4042.20150049**.

61 P. O. Champagne, H. Westwick, A. Bouthillier and M. Sawan, *Nanomedicine*, 2018, **13**, 1385–1400, DOI: **10.2217/nnm-2018-0021**.

62 N. A. Datson, S. Bijl, A. Janson, J. Testerink, R. Van Den Eijnde, R. Weij, J. Puoliväli, K. Lehtimäki, T. Bragge, T. Ahtoniemi and J. C. Van Deutekom, *Nucleic Acid Ther.*, 2020, **30**, 50–65, DOI: **10.1089/nat.2019.0824**.

63 G. Schumann, *et al.*, *Clin. Chem. Lab. Med.*, 2002, **40**, 734–738, DOI: **10.1515/CCLM.2002.126**.

64 G. J. Mangos, J. A. Whitworth, P. M. Williamson and J. J. Kelly, *Nephrology*, 2003, **8**, 267–273, DOI: **10.1111/j.1440-1797.2003.00215.x**.

65 Y. Xie, W. Hou, X. Song, Y. Yu, J. Huang, X. Sun, R. Kang and D. Tang, *Cell Death Differ.*, 2016, **23**, 369–379, DOI: **10.1038/cdd.2015.158**.

66 S. J. Walton, *Disorders of voluntary muscle*, New York, 5th edn, 1988.

67 M. D. Grounds, J. R. Terrill, B. A. Al-Mshhdani, M. N. Duong, H. G. Radley-Crabb and P. G. Arthur, *Dis. Model. Mech.*, 2020, **13**, 1–12, DOI: **10.1242/DMM.043638**.

68 C. G. Carlson and R. V. Makiejus, *Muscle Nerve*, 1990, **13**, 480–484, DOI: **10.1002/mus.880130603**.

69 The Jackson Laboratory, B10.mdx Physiological Data, **https://www.jax.org/jax-mice-and-services/preclinical-research-services/neurobiology-services/muscular-dystrophy-efficacy-studies/b10-mdx#**, (accessed 6 November 2024).

70 G. Liu, P. Lipari, A. Mollin, S. Jung, I. Teplova, W. Li, L. Ying, V. More, W. Lennox, S. Yeh, E. McGann, Y. C. Moon, C. Rice, E. Huarte, B. Gruszka, B. Ray, E. Goodwin, P. Buckendahl, E. Yurkow, B. Braughton, J. Narasimhan, E. Welch, G. Voronin and M. Weetall, *Hum. Mol. Genet.*, 2024, **33**, 211–223, DOI: **10.1016/0002-9343(81)90363-6**.